# N and Ti adatom dynamics on stoichiometric polar TiN(111) surfaces

D.G. Sangiovanni [a,*], F. Tasnádi [a], L. Hultman [a], I. Petrov [a,b], J.E. Greene [a,b], V. Chirita [a]

[a] Department of Physics, Chemistry, and Biology, (IFM) Linköping University, SE-58183 Linköping, Sweden
[b] Departments of Materials Science, Physics, and the Frederick Seitz Materials Research Laboratory, University of Illinois, Urbana, IL 61801, USA

## ARTICLE INFO

## ABSTRACT

We use molecular dynamics (MD) based on the modified embedded atom method (MEAM) to determine diffusion coefficients and migration pathways for Ti and N adatoms ($Ti_{ad}$ and $N_{ad}$) on TiN(111). The reliability of the classical model-potential is verified by comparison with density functional theory (DFT) results at 0 K. MD simulations carried out at temperatures between 600 and 1800 K show that both $Ti_{ad}$ and $N_{ad}$ favor fcc surface sites and migrate among them by passing through metastable hcp positions. We find that $N_{ad}$ species are considerably more mobile than $Ti_{ad}$ on TiN(111); contrary to our previous results on TiN(001). In addition, we show that lattice vibrations at finite temperatures strongly modify the potential energy landscape and result in smaller adatom migration energies, $E_a = 1.03$ for $Ti_{ad}$ and 0.61 eV for $N_{ad}$, compared to 0 K values $E_{a0K} = 1.55$ ($Ti_{ad}$) and 0.79 eV ($N_{ad}$). We also demonstrate that the inclusion of dipole corrections, neglected in previous DFT calculations, is necessary in order to obtain the correct formation energies for polar surfaces such as TiN(111).

## 1. Introduction

Transition-metal (TM) nitride thin films are presently utilized in a wide variety of applications [1–5] based upon their unique properties: high hardness [6–8], excellent scratch and abrasion resistance [9,10], relatively low coefficient of friction [11–13], high-temperature oxidation resistance [14,15], metallic to semiconducting conductivity [16,17], optical absorption which can be tuned across the visible spectrum [16], and superconductivity [18,19]. Recently, TM nitride films with high toughness, the combination of hardness and ductility, have also been synthesized [20–23].

During thin-film deposition, nanostructural and surface morphological evolution [24,25] are largely controlled by the dynamics of adatom surface migration which, in turn, determine nucleation kinetics and film growth modes. The paucity of experimental data on surface dynamics stems from the fact that advanced atomic-scale experimental techniques such as scanning tunneling microscopy (STM) [26–28] and low-energy electron microscopy [29–31], cannot, because of the timescales involved, provide detailed information on atomistic processes governing the initial stages of nucleation and film growth. Thus, computational investigations are necessary to complement experimental data.

*Ab initio* investigations focusing on atomic diffusion on TM nitride surfaces have been used to predict minimum energy paths and corresponding migration energy barriers at 0 K [32–35]. However, the rate of thermally-activated migration events depends not only on diffusion

barriers, but also on jump attempt frequencies [36]. Both are affected by atomic vibrations at finite temperatures [37,38]. Moreover, mass transport properties estimated by 0 K calculations are not reliable for TM nitride systems such as cubic VN which is stable at room temperature [39] due to a large vibrational entropy contribution to the Gibbs free-energy of formation [40], but dynamically unstable (imaginary phonon frequencies) below 240 K [40]. Molecular dynamics (MD), which inherently resolves the problems mentioned above by integrating Newton's equation of motion for each atom, is the primary computational tool for evaluating jump rates and diffusion paths at finite temperatures and revealing the occurrence of non-intuitive atomistic processes [41,42].

Recently, we carried out classical MD (CMD) simulations based on the modified embedded atom method (MEAM) empirical potential to probe intralayer [42–44] and interlayer [45,46] mass transport on, as well as the dynamics of $N_2$ desorption from, TiN(001) surfaces [42]. CMD simulations based upon the MEAM potential model have also been used to investigate point-defect formation and diffusion in bulk TiN [41]. The CMD predictions were validated by *ab initio* MD results [41,42,44].

For TiN, the (001) surface has the lowest formation energy [32,47]. However, the preferred orientation of polycrystalline TiN thin films has been shown experimentally to be controlled more by growth kinetics and synthesis conditions than by thermodynamics [48–51]. Reactive magnetron sputter deposition of TiN on amorphous substrates results primarily in the competitive growth of [001] and [111] oriented grains [50,52,53]. TiN(111) surface energies and layer relaxations, as well as Ti and N adatom ($Ti_{ad}$ and $N_{ad}$) adsorption and migration energies,

* Corresponding author: Tel. +46 13282623; fax +46 13137568.
E-mail address: davsan@ifm.liu.se (D.G. Sangiovanni).

have previously been estimated by 0 K density functional theory (DFT) calculations employing different exchange and correlation energy approximations [32,34,35,47,54–56]. To our knowledge, however, the effects of temperature on TiN(111) mass transport dynamics have not been investigated.

Here, we probe the mass transport properties and polarization of stoichiometric TiN(111) surfaces. CMD simulations, benchmarked by DFT results, are used to evaluate $Ti_{ad}$ and $N_{ad}$ diffusion coefficients as a function of temperature. We find that on TiN(111), $Ti_{ad}$ mobilities are greatly reduced compared to those on TiN(001) [44]. In contrast, $N_{ad}$ species are considerably more mobile on TiN(111) than on TiN(001); in the latter case, nitrogen diffusivities at typical film growth temperatures are limited by $N_2$ desorption, in which the desorbing molecules are primarily composed of N adatoms and N surface atoms [42]. Our CMD results also show that lattice vibrations at temperatures between 600 and 1800 K yield reduced adatom jump activation energies compared to 0 K MEAM and DFT values, confirming the importance of including thermal effects in modeling adatom transport.

Even though the use of periodic boundary conditions generates unphysical dipole–dipole interactions between [111] slab replicas, dipole corrections have been neglected in previous DFT calculations of polar TM nitride and carbide (111) surface properties [47,54]. We show that accounting for this correction results in a significant reduction in calculated Ti- and N-terminated TiN(111) surface energies.

## 2. Computational details

DFT calculations are performed using the VASP code [57] implemented with the projector augmented wave method [58]. Electronic exchange and correlation energies $E_{xc}$ are accounted for with the generalized gradient approximation (GGA) of Perdew and Wang [59] and the local density approximation (LDA). The results obtained with local (LDA) and semi-local (GGA) functionals are compared due to the sensitivity of DFT-estimated surface properties on the $E_{xc}$ approximation [47,60,61]. We employ a plane-wave energy cutoff of 400 eV and sample the Brillouin zone on $5 \times 5 \times 1$ Γ-centered k-point grids to evaluate the total energy to within an accuracy of $10^{-5}$ eV/atom. Densities of states (DOS) and charge-transfer maps, obtained by subtracting atomic electron densities from the self-consistent electron density, are evaluated on $7 \times 7 \times 1$ k-point grids.

CMD simulations are carried out via the large-scale atomic/molecular massively parallel simulator (LAMMPS) [62] by describing atomic interactions with the second-neighbor MEAM potential [63]. The TiN MEAM-parameterization which we recently developed [43] yields CMD TiN(001) surface mass transport properties in excellent agreement with AIMD predictions [42,44] and consistent with experimental determination of surface properties governing crystal growth [43,45,46]. The simulations are performed within the canonical ensemble NVT, with temperature controlled by the Nose thermostat, while integrating the equations of motion at 1 fs time intervals. During all CMD runs, atoms in the bottom two layers (see supercell descriptions below) are fixed at bulk positions. This does not affect the substrate temperature, which depends only on atomic-motion translational degrees of freedom. Prior to initiating each CMD simulation, thermal oscillations in the simulation slab are allowed to stabilize for three ps; a time interval sufficient to equilibrate the system.

CMD/MEAM and DFT TiN(111) supercells are comprised of $6 \times 6$ surface atoms and six layers for a total of 216 atoms. The lateral size of the simulation slab is large enough to avoid adatom self-interactions. In classical simulations, the supercell periodicity is removed along the direction orthogonal to the surface. For DFT calculations, ten vacuum layers separate supercell replicas along [111]. The periodic boundary conditions built into VASP induce artificial dipole/dipole interactions between polar TiN(111) slab replicas. Consequently, both forces and total energies converge slowly with supercell sizes. In order to eliminate this artifact [64,65], a liner electrostatic potential is added to the local

electrostatic potential in all DFT calculations (the tag LDIPOL = .TRUE. is inserted into the VASP input file). At each simulation temperature, the average in-plane interatomic spacing $\sqrt{2} \times d_{NN}$ (see Fig. 1) is obtained, accounting for the experimental TiN thermal expansion coefficient $9 \times 10^{-6}$ $K^{-1}$ [66–68], by rescaling the 0 K bulk Ti–N nearest neighbor distance $d_{NN}$. Rescaling $d_{NN}$ as a function of temperature is necessary to avoid spurious substrate strain effects on adatom jump rates [69].

### 2.1. Surface and adatom adsorption energies

MEAM and DFT 0 K calculations are employed to estimate adatom adsorption energies, surface relaxation, and surface energies. Diffusion energy barriers and minimum energy paths at 0 K are assessed via the nudged elastic band (NEB) method [70]. Nine and 19 NEB images are used in DFT and MEAM NEB calculations, respectively.

Unrelaxed and relaxed TiN(111) surface formation energies $E_{(111)}^{unrlx/rlx}$ are calculated for stoichiometric polar TiN(111) slabs, terminated by a N layer on one side and a Ti layer on the other, based upon the following expression.

$$E_{111}^{unrlx/rlx} = \left( E_{(slab)}^{unrlx/rlx} - n \times E_{bulk} \right)/(2 \times S), \tag{1}$$

for which $E_{slab}^{unrlx}$ is the total energy of the slab with atoms fixed at their bulk positions, $E_{slab}^{rlx}$ is the total energy of the slab after surface relaxation, n is the number of atoms in the slab, $E_{bulk}$ is the energy per atom of bulk TiN, and S is the slab surface area. Note that the factor 1/2 in Eq. (1) yields an average energy per unit area of N and Ti-terminated TiN(111).

DFT $Ti_{ad}$ and $N_{ad}$ adsorption energies are calculated for four different surface positions on TiN(111): fcc, hcp, bridge, and atop sites (see Fig. 1). Adatoms in fcc surface positions, vertically above third-layer atoms, continue the -a-b-c-a-b-c- stacking sequence of cubic bulk TiN. hcp sites, overlying atoms belonging to the second surface layer, correspond to atomic positions in a hexagonal 111 stacking fault. Adatom adsorption energies are defined as.

$$E_{ads} = E_{(slab+adaton)}^{rlx} - \left( E_{slab}^{rlx} + E_{atom} \right), \tag{2}$$

for which $E_{(slab+adaton)}^{rlx}$ is the total energy of the relaxed slab/adatom system, and $E_{atom}$ is the energy of an isolated spin-polarized Ti or N atom: $E_{Ti}^{GGA} = -2.275$ eV, $E_{Ti}^{LDA} = -2.000$ eV, $E_{N}^{GGA} = -3.007$ eV, and $E_{N}^{LDA} = -2.875$ eV. Spin relaxation is used to determine ground-state spin configurations. DFT + GGA adatom adsorption energy landscapes are probed sampling the fcc→hcp diffusion path at eleven equally-spaced points. MEAM Ti and N adatom adsorption energy landscapes are computed on N- and Ti-terminated TiN(111), respectively, using Eq. (2) by sampling the surface unit cell on $32 \times 32$ point grids. The MEAM total energy of isolated static atoms is zero.

### 2.2. Surface diffusion parameters

We probe $Ti_{ad}$ and $N_{ad}$ kinetics on N- and Ti-terminated TiN(111) surfaces, referred to as TiN(111):N and TiN(111):Ti, respectively. $Ti_{ad}$/ TiN(111):N and $N_{ad}$/TiN(111):Ti diffusion pathways and jump rates are determined as a function of temperature via CMD. Initial $Ti_{ad}$ and $N_{ad}$ positions on TiN(111) are at stable fcc sites (see Fig. 1). Ten statistically-independent CMD simulations of Ti adatom diffusion on TiN(111):N, for a total simulation time of 5 μs, are carried out at 900, 1200, 1500, and 1800 K. Five CMD N adatom diffusion runs on TiN(111):Ti, for a total of 1.2 μs, are performed at temperatures T of 600, 900, 1200, and 1500 K. Sample temperatures are chosen based upon initial test simulations.

A single diffusion event requires an adatom to migrate from a stable fcc site through a metastable hcp position to a stable fcc site (Fig. 1). The total jump rate $k_{tot}$ accounts for all adatom diffusion events. That is, $k_{tot}$
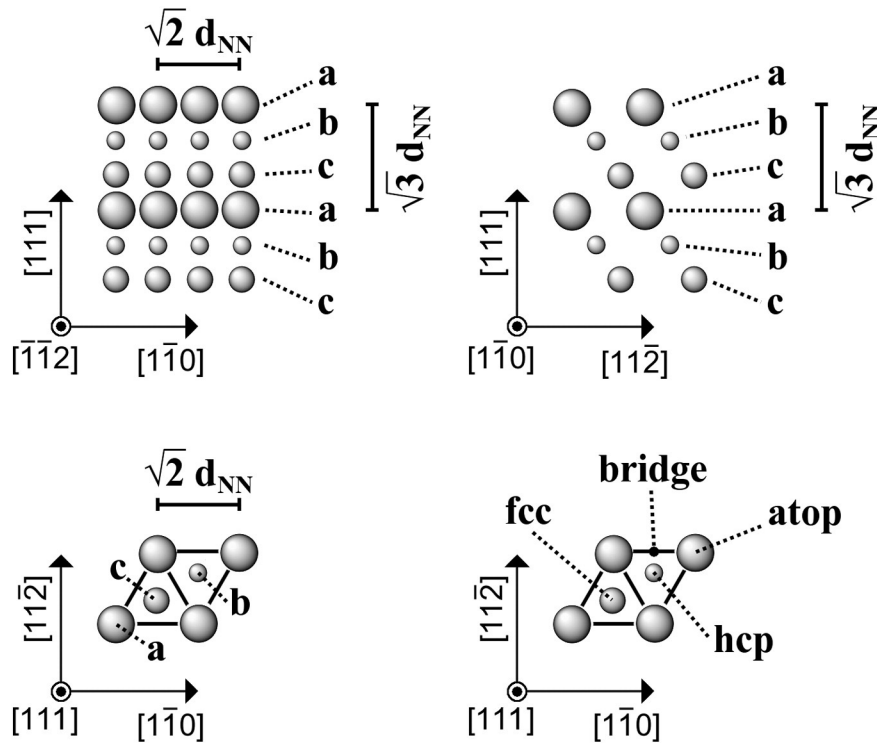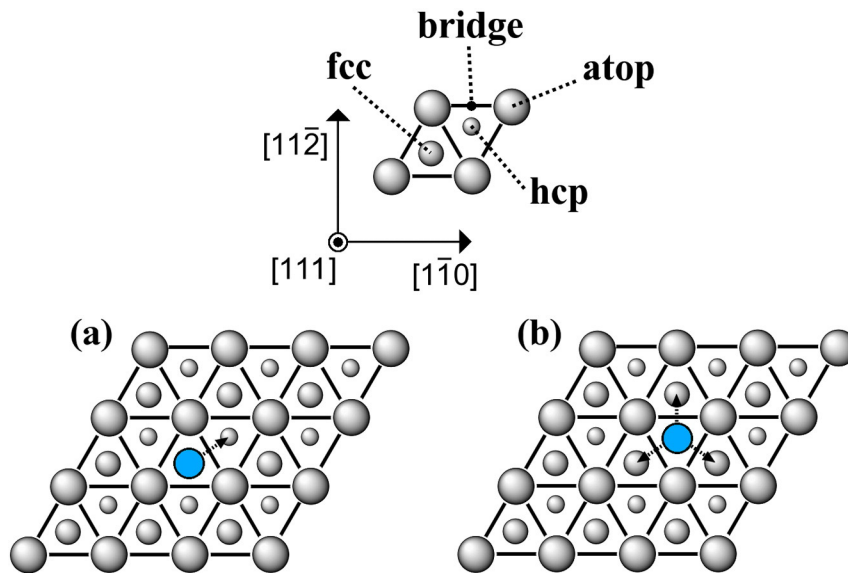
**Fig. 1.** Schematic orthographic representation of [111]-oriented NaCl-structure crystals. Top and bottom panels are side and plan views, respectively. Gray circles of different sizes denote lattice sites of stacking type a, b, and c. $d_{NN}$ is the bulk metal/non-metal nearest neighbor distance. For TiN(111), Ti and N (111) planes alternate with fcc stacking sequence …a-b-c-a-b-c…

includes adatoms jumping back from an hcp to the initial fcc site. Using the jump rates k recorded at different temperatures, we extract jump activation energies $E_a$ and attempt frequencies A via linear interpolation of the Arrhenius equation expressed as $\ln(k_{tot}) = \ln(A) - \frac{E_a}{k_B}\left(\frac{1}{T}\right)$. Assuming fully-uncorrelated jumps and neglecting diffusion events in which adatoms return to their former fcc position (net jump rate $k_{net} = 2k_{tot}/3$) does not affect jump activation energies. However, the attempt frequency corresponding to net migration becomes $A^{net} = 2A^{tot}/3$.

Uncertainties $\sigma_k$, $\sigma_\kappa$, $\sigma_A$, and $\sigma_E$, associated with jump rate values k and $\ln(k)$, attempt frequencies A, and activation energies $E_a$, are determined following the scheme reported in reference [42]. Briefly, $\sigma_E$ and $\sigma_A$ correspond to the widths of $E_a$ and A normal distributions obtained from the linear interpolation of a large number of stochastically-created $\{\ln(k(T_i))\}$ data sets. $\ln[k(T_i)]$ Gaussian distributions are characterized by standard deviations $\sigma_\kappa$.

$Ti_{ad}$ and $N_{ad}$ residence times in metastable hcp sites are sufficiently long to assume equal jump probabilities to any of the three neighboring fcc positions (Fig. 2), including the previously occupied fcc site. The central limit theorem states that, after a time t much larger than the inverse migration rate at a temperature T, a random walk



**Fig. 2.** Schematic orthographic representation of N and Ti adatom diffusion on TiN(111). (a) Starting from a stable fcc site, an adatom (represented by a blue circle) jumps to one of the three neighboring metastable hcp sites, then (b) moves to one of the three neighboring fcc sites. Bridge positions, midpoints between neighboring surface atoms, are transition states along fcc→hcp and hcp→fcc migration paths.

generated by statistically-independent (uncorrelated) consecutive hops, yields a normal distribution probability $p(r,t,T) = [D(T) \times t]^{-3/2} \times \exp[-r^2/(4\,D(T) \times t)]$ for finding the diffusing species at a given distance r from the origin [41,71]. The diffusion coefficient $D(T)$, which on surfaces is related to the width of a bell-shape $p(r, t, T)$ distribution, is expressed as $D(T) = k(T) \times L^2(T)/4$; $k(T)$ and $L(T)$ are adspecies migration rates and jump lengths, respectively, at temperature T. For Ti or N adatoms diffusing among neighboring fcc (111) surface sites, $L(T)$ is equal to $\sqrt{2} \times d_{NN}(T)$. D, evaluated at temperature $T_i$, becomes

$$D(T_i) = k_{net}(T_i) \times d_{NN}^2(T_i)/2. \qquad (3)$$

Uncertainties $\sigma_D$ in $D(T_i)$ diffusion coefficient values are estimated from the expression $\sigma_D(T_i) = \sigma_k(T_i) \times d_{NN}^2(T_i)/2$. Thus, activation energies $E_a'$ and attempt frequencies $A'$ (for which the superscript implies isotropic radial diffusion), with corresponding uncertainties $\sigma_E'$ and $\sigma_A'$, are obtained from interpolation of the complete $\{D(T_i) \pm \sigma_D(T_i)\}$ data set. This leads to the general expression for the temperature-dependent diffusion coefficient:

$$D(T) \times \left[\sigma_D'(T)\right]^{\pm 1} = A' \times \left(\sigma_A'\right)^{\pm 1} \times \exp\left[\left(-E_a' \pm \sigma_E'/\sqrt{2}\right)/(k_B T)\right]. \qquad (4)$$

## 3. Results and discussion

Fig. 3 presents the DOS of unrelaxed and relaxed TiN(111) surfaces. The sharp bulk TiN DOS peak at approximately −15 eV (see Fig. 6 in
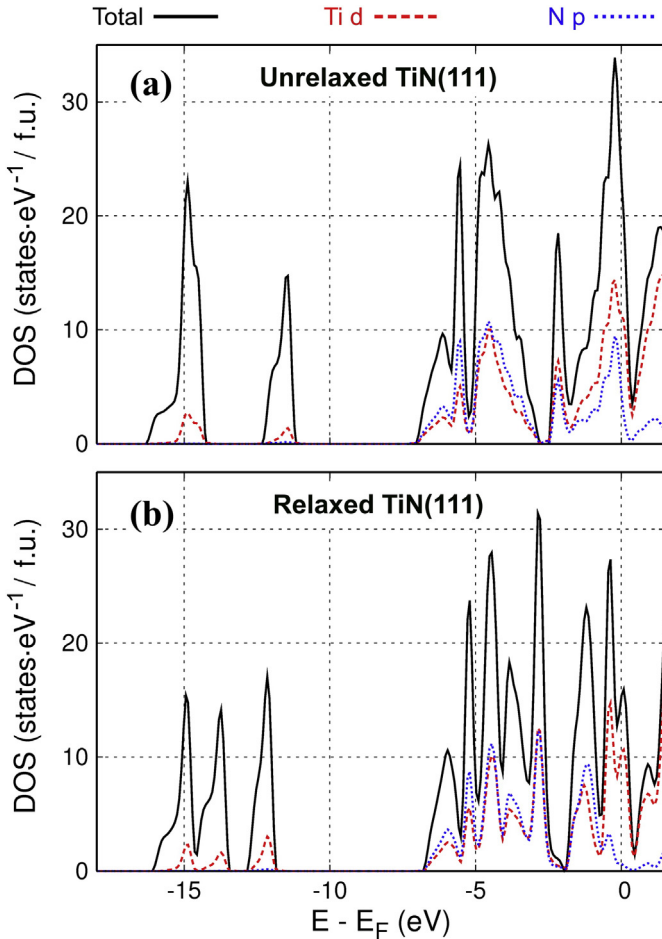


**Fig. 3.** Densities of states per formula unit (f.u.) for (a) unrelaxed and (b) relaxed TiN(111) surfaces obtained from DFT calculations including dipole corrections. Solid black, dashed red, and dotted blue lines correspond to total, d (Ti), and p (N) DOS, respectively.
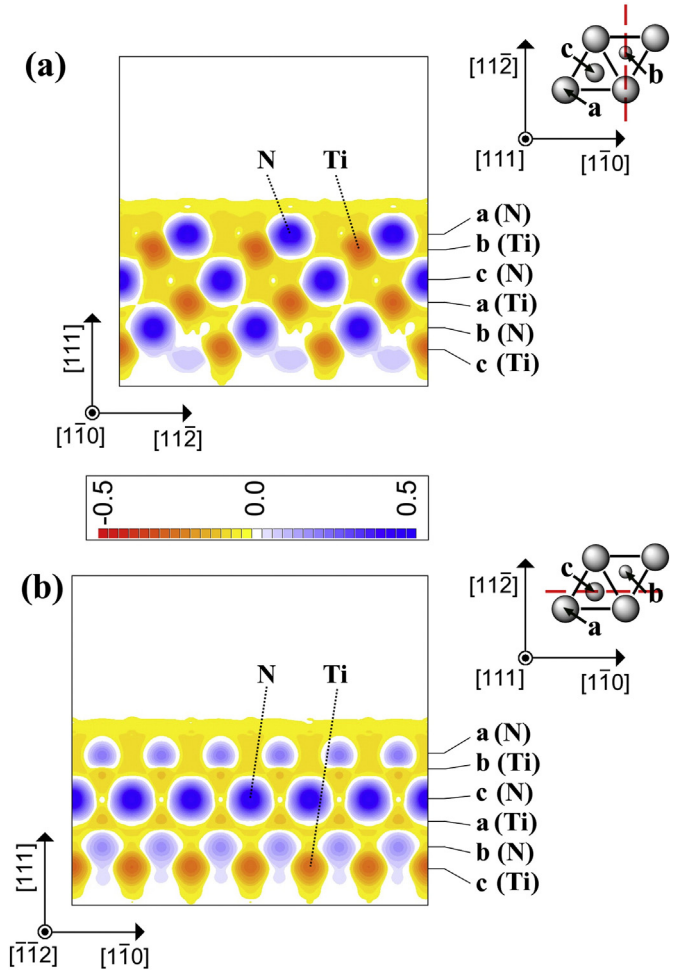


**Fig. 4.** Electron density transfer in relaxed TiN(111). Dashed red lines in the insets (surface plan views) on the right indicate the positions of the charge-density planes viewed end-on: (a) $(1\bar{1}0)$ and (b) $(\bar{1}\bar{1}2)$ The color scale is in units of electrons/Å³.

reference [72]), deriving primarily from 2s(N) states, splits into two peaks separated by an energy gap of ~2 eV in the DOS of unrelaxed TiN(111) (Fig. 3a). Further symmetry reduction due to surface relaxation divides what are nearly energy-degenerate electronic-states close to −15 eV (Fig. 3a) into two DOS peaks centered at −15 and −14 eV (Fig. 3b).

Fig. 4 is a plot of the charge-density transfer driving TiN(111) surface relaxation. The vertical positions of relaxed fcc-stacked (111) layers are indicated by a, b, and c on the right side of the figure. Significant electron accumulation/depletion (blue/yellow) extend from Ti/N-terminated surfaces (note that Ti/N outermost layers are positively/negatively charged) to counterbalance [111] polarization.

As demonstrated by the DOS curves in Fig. 3, both relaxed and unrelaxed six-atomic-layer thick TiN(111) films are metallic, with the Fermi level primarily populated by Ti 3d electrons. Nevertheless, similar to previous reports for polar insulating/semiconducting oxide surfaces

**Table 1**
Dipole moment of unrelaxed and relaxed stoichiometric TiN(111) as calculated by DFT including dipole corrections (see Sec. 2). The simulation slabs are comprised of six atomic layers with surface areas of 5.6 nm² (GGA) and 5.4 nm² (LDA).

| TiN(111) | [111] dipole moment (electrons × Å) | |
|---|---|---|
| | GGA | LDA |
| Unrelaxed | 5.4 | 5.2 |
| Relaxed | 4.0 | 4.2 |

**Table 2**
Comparison between 0 K MEAM and DFT TiN(111) surface energies. Experimental results are also presented for reference.

| | $E(111)$ (meV Å$^{-2}$) | | | Experiment |
|---|---|---|---|---|
| | MEAM | DFT | | |
| Unrelaxed | 245 | 286$^{GGA}$, 351$^{LDA}$, 310$^a$, 306$^b$, 311$^c$, 308$^d$, 317 – 340$^e$ | | - |
| Relaxed | 228 | 206$^{GGA}$, 273$^{LDA}$, 215$^a$, 286$^b$, 226$^c$, 213$^d$, 286 – 309$^e$ | | $E_{(111)} > E_{(011)} \approx 86^{f,g}$ |

a = ref. [32]; b = ref. [54]; c = ref. [55]; d = ref. [56]; e = ref. [47]; f = ref. [78]; g = ref. [79].

[73,74], our DFT results reveal that in conducting TiN(111) layers, the electron reorganization shown in Fig. 4 is not sufficient to cancel [111] polarity. GGA calculations yield total dipole moments of 5.4 for the unrelaxed and 4.0 electrons·Å for the relaxed slabs (surface areas of 5.6 nm$^2$); similar results are obtained with LDA calculations (Table 1). The combination of a non-zero density-of-states at the Fermi level and [111] polarization implies that stoichiometric TiN(111) thin films are electrically conducting within (111) planes, while semiconducting or insulating orthogonal to the slab. The broken lattice periodicity results in energy-level discretization along [111] which inhibits electron flow and prevents polarization cancelation.

The inclusion of dipole corrections in DFT calculations of the properties of polar surfaces is necessary due to the use of periodic boundary conditions which generate fictitious dipole/dipole interactions between adjacent [111] supercell replicas [64,65]. Accounting for the dipole correction results in lowering the GGA TiN(111) surface formation energy $E^{rlx}_{(111)}$ from 221 meV Å$^{-2}$, which is within the range of previous GGA estimations (213–226 meV Å$^{-2}$ [32,55,56]), to 206 meV Å$^{-2}$ (Table 2). An analogous decrease in $E^{rlx}_{(111)}$, ~10%, is obtained with LDA calculations; our dipole-corrected $E^{rlx}_{(111)}$ LDA value, 273 meV Å$^{-2}$, is 32% higher than the result we obtain with GGA (Table 2). In contrast, including dipole corrections results in negligible variations (within ~3%) in surface relaxations, adsorption energies, and adatom diffusion energy barriers on TiN(111) surfaces determined via DFT.

Table 3 presents a comparison of 0 K MEAM and DFT Ti- and N-terminated TiN(111) structural properties. The experimental TiN lattice constant $a_{TiN}$, 4.242 Å [75], is one of the parameters in the MEAM potential. Note that $a_{TiN}$ is slightly overestimated by DFT + GGA and underestimated by DFT + LDA calculations (Table 3). MEAM and DFT results for TiN(111) surface relaxation are in qualitative agreement, but differ quantitatively. Both classical and *ab initio* methods predict shorter surface/second-layer distances $d_{1,2}$, compared to the bulk TiN (111) interlayer spacing $d_{111}$, for both Ti- and N-terminated surfaces. DFT + GGA and DFT + LDA results indicate that $d_{1,2}$ decreases by ~10% for TiN(111):Ti and by ~35% for TiN(111):N. In contrast, MEAM predicts a more pronounced surface relaxation for TiN(111):Ti (−18%) than for TiN(111):N (−9%).

The discrepancy between classical and *ab initio* results for Ti- and N-terminated TiN(111) surface relaxations is explained by the fact that charge reorganization, which controls relaxation, is not directly accounted for within the MEAM formalism. DFT charge-transfer maps show that electron distributions in the vicinity of Ti and N ions in inner TiN(111) layers are similar to those observed in bulk TiN (compare Fig. 4 with Fig. 10 in Ref. [76]), while the charge-density

**Table 3**
Comparison between 0 K MEAM and DFT TiN(111) structural properties. The Ti–N nearest neighbor distance, $d_{NN}$, is half the TiN lattice parameter $a_{TiN}$. Experimental results are also presented for reference.

| TiN structural properties | MEAM | DFT | Experiment |
|---|---|---|---|
| **Bulk parameters (Å)** | | | |
| $d_{NN}$ | 2.121 | 2.128$^{GGA}$, 2.093$^{LDA}$, 2.130$^a$, 2.129$^b$ | 2.120$^c$ |
| (111) interlayer spacing $d_{111}$ | 1.225 | 1.228$^{GGA}$, 1.208$^{LDA}$, 1.230$^a$, 1.229$^b$ | 1.224$^c$ |
| **Interlayer spacing $d_{1,2}$ (Å)** | | | |
| TiN(111):Ti | 1.01 (−18%) | 1.12 (−9%)$^{GGA}$, 1.11 (−8%)$^{LDA}$, 1.11 (−10%)$^a$, 1.08 (−12%)$^b$ | – |
| TiN(111):N | 1.12 (−9%) | 0.82 (−33%)$^{GGA}$, 0.82 (−32%)$^{LDA}$, 0.78 (−37%)$^a$, 0.79 (−36%)$^b$ | – |
| **Interlayer thickness $d_{1,3}$ (Å)** | | | |
| TiN(111):Ti | 2.27 (−7%) | 2.40 (−2%)$^{GGA}$, 2.36 (−2%)$^{LDA}$ | – |
| TiN(111):N | 2.40 (−2%) | 2.34 (−5%)$^{GGA}$, 2.30 (−5%)$^{LDA}$ | 2.4 (−2%)$^d$ |

a = ref. [32]; b = ref. [56]; c = ref. [75]; d = ref. [77].

**Table 4**
Comparison between DFT and MEAM adatom adsorption energies $E_{ads}$ and migration energy barriers $E_{a0}$ on TiN(111) at 0 K. GGA and LDA superscripts indicate DFT results of the present work; these account for dipole corrections.

| *Static* TiN(111) | Ti$_{ad}$/TiN(111):N | | N$_{ad}$/TiN(111):Ti | |
|---|---|---|---|---|
| | MEAM | DFT | MEAM | DFT |
| **$E_{ads}$ (eV)** | | | | |
| fcc | −8.17 | −11.47$^{GGA}$, −13.56$^{LDA}$, −12.54$^a$, −10.09$^b$, −9.92$^c$ | −6.63 | −8.10$^{GGA}$, −9.05$^{LDA}$, −8.33$^a$, −7.99$^c$, −7.61$^d$ |
| hcp | −7.35 | −10.45$^{GGA}$, −12.45$^{LDA}$, −11.31$^b$, −9.13$^b$, −8.97$^c$ | −6.26 | −7.32$^{GGA}$, −8.25$^{LDA}$, −7.65$^a$, −7.37$^c$, −7.04$^d$ |
| bridge | −6.65 | −9.71$^{GGA}$, −11.75$^{LDA}$, −10.64$^a$, −8.35$^b$, −8.26$^c$ | −5.91 | −7.06$^{GGA}$, −7.99$^{LDA}$, −7.32$^a$, −7.13$^c$, −6.37$^d$ |
| atop | −3.29 | −7.82$^{LDA}$, −7.13$^a$ | −4.22 | −5.50$^{LDA}$, −4.80$^a$, −4.47$^d$ |
| $E_{ads}$(hcp)–$E_{ads}$(fcc) | 0.82 | 1.02$^{GGA}$, 1.11$^{LDA}$, 1.23$^a$, 0.96$^b$, 0.95$^c$ | 0.37 | 0.78$^{GGA}$, 0.80$^{LDA}$, 0.68$^a$, 0.62$^c$, 0.57$^d$ |
| **NEB diffusion barrier* $E_{a0K}$ (eV)** | | | | |
| fcc→hcp | 1.55 | 1.76$^{GGA}$, 1.80$^{LDA}$, 1.91$^a$, 1.74$^b$, 1.66$^c$ | 0.79 | 1.04$^{GGA}$, 1.06$^{LDA}$, 1.01$^a$, 0.86$^c$, 1.24$^d$ |
| hcp→fcc | 0.48 | 0.74$^{GGA}$, 0.70$^{LDA}$, 0.67$^a$, 0.78$^b$, 0.71$^c$ | 0.34 | 0.26$^{GGA}$, 0.26$^{LDA}$, 0.32$^a$, 0.24$^c$, 0.67$^d$ |

*If not calculated directly in the references, (fcc → hcp) and (hcp → fcc) diffusion energy barriers are approximated as [$E_{ads}$(bridge) – $E_{ads}$(fcc)] and [$E_{ads}$(bridge) – $E_{ads}$(hcp)], respectively.
a = ref. [35]; b = ref. [32]; c = ref. [34]; d = ref. [54]; f = ref. [56].

**(a)**



**(b)**
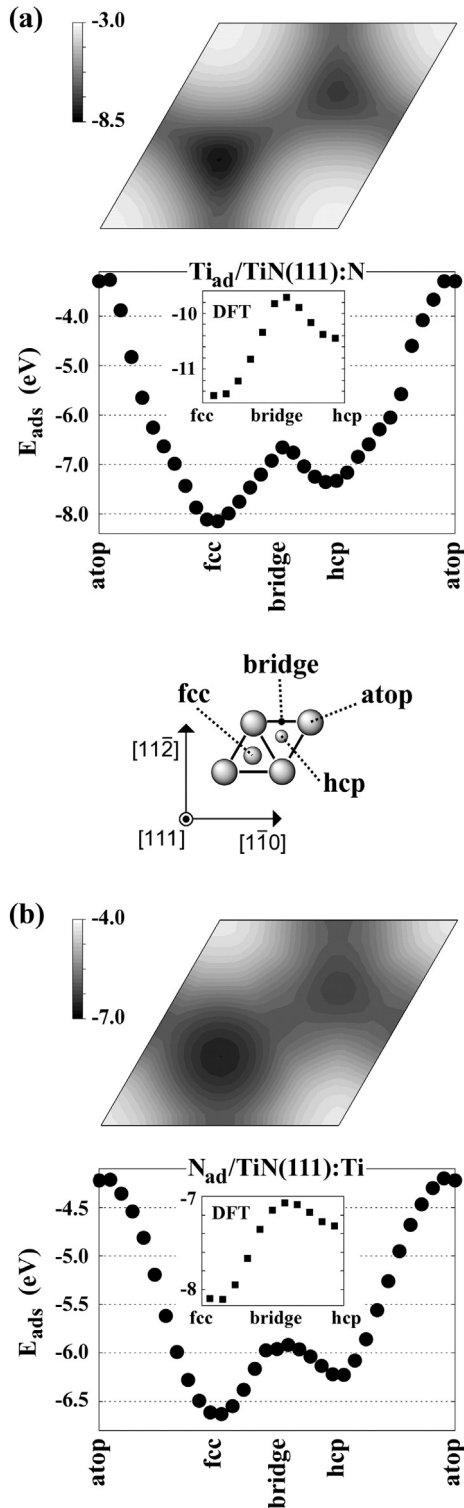


**Fig. 5.** Plan view of 0 K MEAM adsorption energy landscapes for (a) Ti and (b) N adatoms on TiN(111). The adsorption energy profile curves are calculated for a straight path from atop→fcc→bridge→hcp→atop positions. The insets show the results obtained by DFT + GGA including dipole corrections for fcc→hcp adatom migration paths. The gray scale is in units of eV.

surrounding N and Ti surface ions exhibit significantly different shapes. Since MEAM calculates the forces acting on (111) nitrogen and titanium layers by assuming that each ion is embedded in a background electron density with cubic-B1 point-group symmetry, as in bulk TiN (MEAM reference structure), relaxation of the outermost TiN(111) layers is not accurately reproduced.
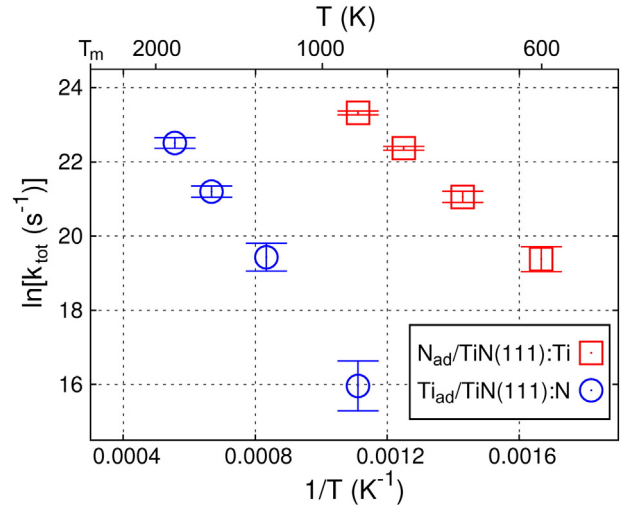


**Fig. 6.** CMD Ti and N adatom total jump rate $\ln(k_{tot})$ dependence on inverse temperature $1/T$. The melting point of TiN is $T_m = 2930\ °C = 3200$ K. Error bars indicate jump rate uncertainties $\sigma_\kappa$.

Despite the rather poor agreement between MEAM and DFT surface monolayer heights $d_{1,2}$ (see Table 3), Ti-N and N-Ti bilayer thicknesses $d_{1,3}$ predicted by MEAM, 2.27 Å for TiN(111):Ti and 2.40 Å for TiN(111):N, are consistent with DFT values: 2.36–2.40 Å for TiN(111):Ti and 2.30–2.34 Å for TiN(111):N, and in excellent agreement with STM measurements: ~2.4 Å for N-terminated TiN(111) [77] (Table 3). In addition, the surface energy of relaxed stoichiometric TiN(111) obtained by MEAM, 228 meV Å$^{-2}$, is within the range of DFT results which vary from 206 to 309 meV Å$^{-2}$ (Table 2). The relationship among MEAM TiN (111), (011), and (001) surface energies $E_{(111)} = 228$, $E_{(011)} = 160$, and $E_{(001)} = 90$ meV Å$^{-2}$ [43], is consistent with experimental results: $E_{(111)} > E_{(011)} \approx E_{(001)}/0.8 = 86$ meV Å$^{-2}$ [78,79].

Table 4 lists MEAM and DFT-determined $Ti_{ad}$ and $N_{ad}$ adsorption energies $E_{ads}$ on TiN(111), together with 0 K migration energy barriers $E_{a0K}$ obtained from NEB calculations. DFT adsorption energies for adatoms in stable fcc surface sites are between $-9.92$ and $-13.56$ eV for $Ti_{ad}$/TiN(111):N and $-7.61$ and $-9.05$ eV for $N_{ad}$/TiN(111):Ti. MEAM $E_{ads}$ values are close to *ab initio* $E_{ads}$ ranges: $E_{ads} = -8.17$ and $-6.63$ eV for $Ti_{ad}$ and $N_{ad}$, respectively. The scatter in DFT values is often due to calculations employing different accuracies (e.g. k-point grid thicknesses and basis set cutoff energies), supercell sizes and/or relaxation methods, as well as basis sets (e.g. linearly augmented plane waves, plane waves, etc.). However, it has been proven that local and semi-local exchange and correlation approximations, typically implemented in DFT, possess an intrinsic flaw which limits their accuracy in describing adsorption energies and surface formation energies [60,61]. This problem is reflected by the large deviations (~30% for $E_{(111)}$, Table 2, and ~20% for $E_{ads}$, Table 4) between DFT + LDA and DFT + GGA values obtained in the present work. Considering the uncertainty associated with DFT values, the agreement between classical and *ab initio* $E_{ads}$ results is quite reasonable.

Fig. 5 shows the 0 K MEAM adsorption energy landscape for $Ti_{ad}$ (Fig. 5a) and $N_{ad}$ (Fig. 5b) on N- and Ti-terminated TiN(111) surfaces, respectively. $E_{ads}$ values are plotted along $\langle 11\bar{2}\rangle$ as the adatom moves from atop to fcc to bridge to hcp to atop sites. MEAM adsorption energy profiles are consistent with DFT + GGA results (see insets in Fig. 5). The plots show that both $Ti_{ad}$ and $N_{ad}$ favor TiN(111) fcc positions, and diffuse among them by passing through metastable hcp sites (Fig. 2). The transition state along the minimum energy migration path is located near surface bridge sites (Fig. 2). Surface atop positions, i.e., a N (Ti) adatom on top of a Ti (N) surface atom, are unstable.
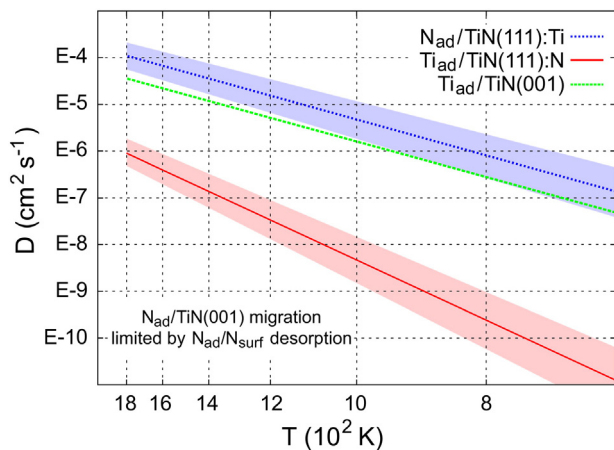
**Table 5**
$Ti_{ad}/TiN(111)$:N and $N_{ad}/TiN(111)$:Ti adatom jump activation energies $E_a$, attempt frequencies A, and corresponding isotropic/radial diffusion parameters $E_a'$ and A' as determined via CMD simulations. MEAM + NEB 0 K migration energies are shown for comparison.

| Adatom diffusivity | CMD (600–1800 K) | MEAM + NEB (0 K) |
|---|---|---|
| $Ti_{ad}/TiN(111)$:N | | |
| $E_a$ (eV) | $1.02 \pm 0.10$ | 1.55 |
| $A^{tot}$ ($10^{13}$ s$^{-1}$) | 0.41 ($\times 2.4^{\pm 1}$) | |
| $E_a'$ (eV) | $1.03 \pm 0.09$ | |
| A' (cm$^2$ s$^{-1}$) | 6.46 ($\times 2.3^{\pm 1}$) $\times 10^{-4}$ | |
| $N_{ad}/TiN(111)$:Ti | | |
| $E_a$ (eV) | $0.61 \pm 0.05$ | 0.79 |
| $A^{tot}$ ($10^{13}$ s$^{-1}$) | 3.70 ($\times 2.1^{\pm 1}$) | |
| $E_a'$ (eV) | $0.61 \pm 0.05$ | |
| A' (cm$^2$ s$^{-1}$) | 5.69 ($\times 2.1^{\pm 1}$) $\times 10^{-3}$ | |

The primary parameter which controls adatom mobilities on TiN(111) is the diffusion energy-barrier $E_a$ along the path from stable fcc to metastable hcp sites. 0 K DFT calculations predict energy barriers $E_{a0K}$ ranging from 1.66 to 1.91 eV for $Ti_{ad}/TiN(111)$:N migration and from 0.86 to 1.24 eV for $N_{ad}/TiN(111)$:Ti migration [32,34,35,54] (Table 4). Although DFT + GGA calculations systematically predict smaller TiN(111) surface formation energies than DFT + LDA (Table 2), the LDA $E_{a0K}$ values are within GGA ranges (Table 4). Considering the wide scatter of DFT $E_{a0K}$ values, 0 K MEAM + NEB estimates, $E_{a0K} = 1.55$ eV for Ti and $E_{a0K} = 0.79$ eV for N adatoms, are reasonable and validate the use of the classical potential with our TiN MEAM parameters [43] for the evaluation of adatom diffusion coefficients via CMD.

At temperatures between 600 and 1800 K, CMD simulations show that Ti and N adatoms on TiN(111) favor fcc surface sites and migrate among these sites by transiting through metastable hcp positions (Fig. 2), as for the 0 K results. Adatom long jumps, i.e. jumps yielding migration distances corresponding to two or more single jumps in the same direction, previously reported for $Ti_{ad}$ migration on TiN(001) [43,44], are never observed. From linear interpolation of adatom total jump rates $k_{tot}$ vs. inverse temperature 1/T, Fig. 6, we determine activation energies $E_a = 1.02 \pm 0.10$ eV and attempt frequencies $A^{tot} = 0.41(\times 2.4^{\pm 1}) \times 10^{13}$ s$^{-1}$ for $Ti_{ad}/TiN(111)$:N, and $E_a = 0.61 \pm 0.05$ eV with $A^{tot} = 3.70(\times 2.1^{\pm 1}) \times 10^{13}$ s$^{-1}$ for $N_{ad}/TiN(111)$:Ti migration.



**Fig. 7.** $Ti_{ad}/TiN(111)$:N and $N_{ad}/TiN(111)$:Ti diffusion coefficients extrapolated using Eqs. (3) and (4) with $E_a'$ and A' values from Table 5. Shaded areas indicate uncertainties in D values. $Ti_{ad}/TiN(001)$ [44] diffusion coefficients are shown for comparison. Note that $N_{ad}/TiN(001)$ diffusion coefficients are negligible due to rapid N adatom/N surface ($N_{ad}/N_{surf}$) pair formation and desorption [42].

CMD and MEAM + NEB $Ti_{ad}$ and $N_{ad}$ diffusion parameters are summarized in Table 5. MEAM adatom 0 K migration energies $E_{a0K}$ are up to 35% larger than adatom jump activation energies $E_a$ obtained via CMD at temperatures between 600 and 1800 K. Lattice-vibration-induced changes in migration energies are also observed for Ti adatoms on TiN(001) [44]. We have previously shown that, although the Ti adatom MEAM migration energy value ($E_{a0K} = 0.8$ eV) on TiN(001) is much larger than that obtained by DFT ($E_{a0K} = 0.43$ eV) [43], density functional MD and CMD simulations yield similar Ti adatom jump activation energies ($E_a = 0.51 \pm 0.03$ eV and $E_a = 0.62 \pm 0.01$ eV, respectively) and jump rates [44]. For N adatom migration on TiN(001), the 0 K DFT value, $E_{a0K} = 0.95$ eV [32,43], is ~35% smaller than the *ab initio* MD result, $E_a = 1.4$ eV [42]. We attribute the change in migration energies to modifications in the effective potential energy landscape induced by lattice vibrations at finite temperatures [80].

$Ti_{ad}$ and $N_{ad}$ diffusion coefficients D(T) on TiN(111) (Fig. 7) are extrapolated from CMD diffusion parameters (Table 5) using Eqs. (3) and (4) at T between 670 and 1800 K. $Ti_{ad}/TiN(001)$ diffusivities are added for comparison [44]. The results show that $N_{ad}$ species are considerably more mobile than $Ti_{ad}$ on TiN(111) at all temperatures (Fig. 7). Moreover, Ti adatoms exhibit much lower diffusivity on TiN(111):N than on TiN(001), for which their migration energy, $E_a = 0.60$ eV (obtained from the rate of uncorrelated jumps) [44], is almost a factor of two smaller. In contrast, N adatoms exhibit higher diffusivities on TiN(111):Ti than on TiN(001) due, in the latter case, to the combination of a high migration energy, ~1.4 eV, and $N_2$ molecule formation and desorption rates being ~1/4 that of adatom jump rates [42].

## 4. Conclusions

Classical MEAM 0 K predictions for TiN(111) surface relaxation and formation energies, as well as N and Ti adatom adsorption energies, migration paths and energy barriers on TiN(111) are validated by comparison with DFT calculation results. We demonstrate that accounting for dipole corrections, previously neglected in DFT calculations of the properties of polar stoichiometric TiN(111), reduces the surface energy by 10%. CMD simulations, carried out over the temperature range 600–1800 K, show that N and Ti adatoms favor fcc adsorption sites on TiN(111), and migrate among them by crossing metastable hcp sites. Calculated adatom activation energies $E_a$ and attempt frequencies A are $E_a = 0.61 \pm 0.05$ eV and $A = 3.70(\times 2.1^{\pm 1}) \times 10^{13}$ s$^{-1}$ for N/TiN(111):Ti migration, and $E_a = 1.02 \pm 0.10$ eV and $A = 0.41(\times 2.4^{\pm 1}) \times 10^{13}$ s$^{-1}$ for Ti/TiN(111):N migration, respectively. Corresponding adatom diffusion coefficients are obtained from surface distribution probabilities assuming fully-uncorrelated jumps. CMD $E_a$ values are considerably smaller than $E_{a0K}$ estimated by 0 K MEAM + NEB calculations due to modifications in the effective potential energy landscape induced by lattice vibrations at finite temperatures. These results confirm the importance of including thermal effects in theoretical determinations of surface diffusion parameters.

# References

[1] J.M. Molarius, A.S. Korhonen, E. Harju, R. Lappalainen, Surf. Coat. Technol. 33 (1987) 117.
[2] J.S. Chun, I. Petrov, J.E. Greene, J. Appl. Phys. 86 (1999) 3633.
[3] P. Patsalas, N. Kalfagiannis, S. Kassavetis, Materials 8 (2015) 3128.
[4] C. Mitterer, F. Holler, D. Reitberger, E. Badisch, M. Stoiber, C. Lugmair, R. Nobauer, T. Muller, R. Kullmer, Surf. Coat. Technol. 163 (2003) 716.
[5] M. Mühlbacher, A.S. Bochkarev, F. Mendez-Martin, B. Sartory, L. Chitu, M.N. Popov, P. Puschnig, J. Spitaler, H. Ding, N. Schalk, J. Lu, L. Hultman, C. Mitterer, J. Appl. Phys. 118 (2015) 085307.
[6] C.S. Shin, D. Gall, N. Hellgren, J. Patscheider, I. Petrov, J.E. Greene, J. Appl. Phys. 93 (2003) 6025.
[7] T. Reeswinkel, D.G. Sangiovanni, V. Chirita, L. Hultman, J.M. Schneider, Surf. Coat. Technol. 205 (2011) 4821.
[8] G. Abadias, L.E. Koutsokeras, S.N. Dub, G.N. Tolmachova, A. Debelle, T. Sauvage, P. Villechaise, J. Vac. Sci. Technol. A 28 (2010) 541.
[9] P. Hedenqvist, M. Bromark, M. Olsson, S. Hogmark, E. Bergmann, Surf. Coat. Technol. 63 (1994) 115.
[10] B.D. Beake, V.M. Vishnyakov, A.J. Harris, Tribol. Int. 44 (2011) 468.
[11] T. Polcar, T. Kubart, R. Novak, L. Kopecky, P. Siroky, Surf. Coat. Technol. 193 (2005) 192.
[12] K. Kutschej, P.H. Mayrhofer, M. Kathrein, P. Polcik, C. Mitterer, Surf. Coat. Technol. 188 (2004) 358.
[13] G. Gassner, P.H. Mayrhofer, K. Kutschej, C. Mitterer, M. Kathrein, Surf. Coat. Technol. 201 (2006) 3335.
[14] A.S. Ingason, F. Magnus, J.S. Agustsson, S. Olafsson, J.T. Gudmundsson, Thin Solid Films 517 (2009) 6731.
[15] D. McIntyre, J.E. Greene, G. Hakansson, J.E. Sundgren, W.D. Munz, J. Appl. Phys. 67 (1990) 1542.
[16] D. Gall, I. Petrov, J.E. Greene, J. Appl. Phys. 89 (2001) 401.
[17] L.E. Koutsokeras, G. Abadias, C.E. Lekka, G.M. Matenoglou, D.F. Anagnostopoulos, G.A. Evangelakis, P. Patsalas, Appl. Phys. Lett. 93 (2008) 011904.
[18] H.S. Seo, T.Y. Lee, I. Petrov, J.E. Greene, D. Gall, J. Appl. Phys. 97 (2005) 083521.
[19] A.B. Mei, A. Rockett, L. Hultman, I. Petrov, J.E. Greene, J. Appl. Phys. 114 (2013) 193708.
[20] H. Kindlund, D.G. Sangiovanni, L. Martinez-de-Olcoz, J. Lu, J. Jensen, J. Birch, I. Petrov, J.E. Greene, V. Chirita, L. Hultman, APL Mater. 1 (2013) 042104.
[21] H. Kindlund, D.G. Sangiovanni, J. Lu, J. Jensen, V. Chirita, I. Petrov, J.E. Greene, L. Hultman, J. Vac. Sci. Technol. A 32 (2014) 030603.
[22] H. Kindlund, D.G. Sangiovanni, J. Lu, J. Jensen, V. Chirita, J. Birch, I. Petrov, J.E. Greene, L. Hultman, Acta Mater. 77 (2014) 394.
[23] G. Abadias, M.B. Kanoun, S. Goumri-Said, L. Koutsokeras, S.N. Dub, P. Djemia, Phys. Rev. B 90 (2014) 144107.
[24] I. Petrov, P.B. Barna, L. Hultman, J.E. Greene, J. Vac. Sci. Technol. A 21 (2003) S117.
[25] F.H. Baumann, D.L. Chopp, T.D. de la Rubia, G.H. Gilmer, J.E. Greene, H. Huang, S. Kodambaka, P. O'Sullivan, I. Petrov, MRS Bull. 26 (2001) 182.
[26] S. Kodambaka, V. Petrova, A. Vailionis, P. Desjardins, D.G. Cahill, I. Petrov, J.E. Greene, Surf. Rev. Lett. 7 (2000) 589.
[27] S. Kodambaka, V. Petrova, A. Vailionis, P. Desjardins, D.G. Cahill, I. Petrov, J.E. Greene, Thin Solid Films 392 (2001) 164.
[28] S. Kodambaka, V. Petrova, A. Vailionis, I. Petrov, J.E. Greene, Surf. Sci. 526 (2003) 85.
[29] F. Watanabe, S. Kodambaka, W. Swiech, J.E. Greene, D.G. Cahill, Surf. Sci. 572 (2004) 425.
[30] S. Kodambaka, N. Israeli, J. Bareno, W. Swiech, K. Ohmori, I. Petrov, J.E. Greene, Surf. Sci. 560 (2004) 53.
[31] J. Bareno, S. Kodambaka, S.V. Khare, W. Swiech, V. Petrova, I. Petrov, J.E. Greene, TiN surface dynamics: role of surface and bulk mass transport processes, Advanced Summer School in Physics, Mexico City, Mexico 2006, p. 205.
[32] D. Gall, S. Kodambaka, M.A. Wall, I. Petrov, J.E. Greene, J. Appl. Phys. 93 (2003) 9086.
[33] B. Alling, P. Steneteg, C. Tholander, F. Tasnádi, I. Petrov, J.E. Greene, L. Hultman, Phys. Rev. B 85 (2012) 245422.
[34] C. Tholander, B. Alling, F. Tasnádi, J.E. Greene, L. Hultman, Surf. Sci. 630 (2014) 28.
[35] Y. Ren, X.J. Liu, X. Tan, E. Westkamper, Comput. Mater. Sci. 77 (2013) 102.
[36] D.G. Truhlar, B.C. Garrett, S.J. Klippenstein, J. Phys. Chem. 100 (1996) 12771.
[37] H.M. Gilder, D. Lazarus, Phys. Rev. B 11 (1975) 4916.
[38] H. Matzke, Diffusion in Carbides and Nitrides, Kluwer Academic Publ., Dordrecht, 1990.
[39] A.B. Mei, R.B. Wilson, D. Li, D.G. Cahill, A. Rockett, J. Birch, L. Hultman, J.E. Greene, I. Petrov, J. Appl. Phys. 115 (2014) 214908.
[40] A.B. Mei, O. Hellman, N. Wireklint, C.M. Schlepütz, D.G. Sangiovanni, B. Alling, A. Rockett, L. Hultman, I. Petrov, J.E. Greene, Phys. Rev. B 91 (2015) 054101.
[41] D.G. Sangiovanni, B. Alling, P. Steneteg, L. Hultman, I.A. Abrikosov, Phys. Rev. B 91 (2015) 054301.
[42] D.G. Sangiovanni, D. Edström, L. Hultman, I. Petrov, J.E. Greene, V. Chirita, Surf. Sci. 624 (2014) 25.
[43] D.G. Sangiovanni, D. Edström, L. Hultman, V. Chirita, I. Petrov, J.E. Greene, Phys. Rev. B 86 (2012) 155443.
[44] D.G. Sangiovanni, D. Edström, L. Hultman, I. Petrov, J.E. Greene, V. Chirita, Surf. Sci. 627 (2014) 34.
[45] D. Edström, D.G. Sangiovanni, L. Hultman, V. Chirita, I. Petrov, J.E. Greene, Thin Solid Films 558 (2014) 37.
[46] D. Edström, D.G. Sangiovanni, L. Hultman, I. Petrov, J.E. Greene, V. Chirita, Thin Solid Films 589 (2015) 133.
[47] M. Marlo, V. Milman, Phys. Rev. B 62 (2000) 2899.
[48] P.H. Mayrhofer, M. Geier, C. Loecker, L. Chen, Int. J. Mater. Res. 100 (2009) 1052.
[49] S.-S. Yang, Y.-R. Lin, S.-T. Wu, Surf. Coat. Technol. 201 (2007) 4850.
[50] L. Hultman, J.E. Sundgren, J.E. Greene, D.B. Bergstrom, I. Petrov, J. Appl. Phys. 78 (1995) 5395.
[51] U. Helmersson, J.E. Sundgren, J.E. Greene, J. Vac. Sci. Technol. A 4 (1986) 500.
[52] J.E. Greene, J.E. Sundgren, L. Hultman, I. Petrov, D.B. Bergstrom, Appl. Phys. Lett. 67 (1995) 2928.
[53] I. Petrov, L. Hultman, J.E. Sundgren, J.E. Greene, J. Vac. Sci. Technol. A 10 (1992) 265.
[54] A. Vojvodic, C. Ruberto, B.I. Lundqvist, Surf. Sci. 600 (2006) 3619.
[55] S.V. Dudiy, B.I. Lundqvist, Phys. Rev. B 69 (2004) 125421.
[56] S.Q. Hao, B. Delley, C. Stampfl, Phys. Rev. B 74 (2006) 035402.
[57] G. Kresse, J. Hafner, Phys. Rev. B 47 (1993) 558.
[58] P.E. Blöchl, Phys. Rev. B 50 (1994) 17953.
[59] J.P. Perdew, J.A. Chevary, S.H. Vosko, K.A. Jackson, M.R. Pederson, D.J. Singh, C. Fiolhais, Phys. Rev. B 46 (1992) 6671.
[60] L. Schimka, J. Harl, A. Stroppa, A. Gruneis, M. Marsman, F. Mittendorfer, G. Kresse, Nat. Mater. 9 (2010) 741.
[61] P.J. Feibelman, B. Hammer, J.K. Norskov, F. Wagner, M. Scheffler, R. Stumpf, R. Watwe, J. Dumesic, J. Phys. Chem. B 105 (2001) 4018.
[62] S. Plimpton, J. Comput. Phys. 117 (1995) 1.
[63] B.J. Lee, M.I. Baskes, Phys. Rev. B 62 (2000) 8564.
[64] J. Neugebauer, M. Scheffler, Phys. Rev. B 46 (1992) 16067.
[65] see "*Monopole, dipole and quadrupole corrections*" at http://cms.mpi.univie.ac.at/vasp/guide/.
[66] L.E. Toth, Transition Metal Carbides and Nitrides, Academic Press, New York, 1971.
[67] Y. Kumashiro, Electric Refractory Materials, CRC Press, 2000.
[68] D.S. Rickerby, S.J. Bull, A.M. Jones, F.L. Cullen, B.A. Bellamy, Surf. Coat. Technol. 39 (1989) 397.
[69] H. Brune, K. Bromann, H. Roder, K. Kern, J. Jacobsen, P. Stoltze, K. Jacobsen, J. Norskov, Phys. Rev. B 52 (1995) 14380.
[70] G. Henkelman, B.P. Uberuaga, H. Jonsson, J. Chem. Phys. 113 (2000) 9901.
[71] A.I. Khinchin, Mathematical Foundations of Statistical Mechanics, Dover publications, New York, 1949.
[72] D.G. Sangiovanni, V. Chirita, L. Hultman, Phys. Rev. B 81 (2010) 104107.
[73] A. Pojani, F. Finocchi, J. Goniakowski, C. Noguera, Surf. Sci. 387 (1997) 354.
[74] C. Noguera, J. Phys. Condens. Matter 12 (2000) R367.
[75] T. Lee, K. Ohmori, C.S. Shin, D.G. Cahill, I. Petrov, J.E. Greene, Phys. Rev. B 71 (2005) 144106.
[76] D.G. Sangiovanni, L. Hultman, V. Chirita, Acta Mater. 59 (2011) 2121.
[77] S. Kodambaka, S.V. Khare, V. Petrova, D.D. Johnson, I. Petrov, J.E. Greene, Phys. Rev. B 67 (2003) 035409.
[78] L. Hultman, J.E. Sundgren, J.E. Greene, J. Appl. Phys. 66 (1989) 536.
[79] T.C. Chou, J. Appl. Phys. 67 (1990) 2670.
[80] O. Hellman, I.A. Abrikosov, S.I. Simak, Phys. Rev. B 84 (2011), 180301(R).